JOURNAL OF GEOPHYSICAL RESEARCH, VOL. 115, E00E21, doi:10.1029/2010JE003568, 2010

Simulations of atmospheric phenomena at the Phoenix landing site with the Ames General Circulation Model

Steven M. Nelli,[1] Nilton O. Renno,[1] James R. Murphy,[2] William C. Feldman,[3] and Stephen W. Bougher[1]

Received 3 January 2010; accepted 26 January 2010; published 19 June 2010.

[1] Phoenix, the first NASA Mars Scout class mission, was designed to "follow the water" and study the polar region. Landing in late northern spring, Phoenix measured soil chemistry, near-surface water ice, and studied numerous atmospheric properties and weather phenomena. Here, we use atmospheric measurements made by Phoenix to test and calibrate the Ames General Circulation Model (GCM) and start the process of analyzing and interpreting the vast data set provided by this groundbreaking mission. The GCM reproduces surface pressures and temperatures within the measured diurnal and seasonal ranges. It also reproduces measured water ice cloud profiles with ground fogs forming after L_s = 120° and a separate cloud deck between 3 km and 6 km above the surface. Near-surface water vapor pressures have daytime maxima above 1 Pa in both the data and model. We find that frosts and fogs observed by Phoenix are correlated with the formation of high-pressure weather systems over the landing site.

Citation: Nelli, S. M., N. O. Renno, J. R. Murphy, W. C. Feldman, and S. W. Bougher (2010), Simulations of atmospheric phenomena at the Phoenix landing site with the Ames General Circulation Model, *J. Geophys. Res.*, *115*, E00E21, doi:10.1029/2010JE003568.

1. Introduction

[2] Phoenix landed on 25 May 2008 at 68.16°N, 233°E on the plains of Vastitas Borealis [*P. Smith et al.*, 2009]. The objectives of the Phoenix mission were fourfold: (1) to find near-surface sources of water, (2) to study the exchange of water between the regolith and the atmosphere, (3) to look for biosignatures or key elements for life (C, H, O, N, P, and S), and (4) to determine potential life sustaining energy sources available either in the past or the present [*Smith et al.*, 2008]. Phoenix is the most poleward landed spacecraft to date on Mars. Its landing site was chosen because of the discovery of large reservoirs of water ice poleward of 60° latitude [*Feldman et al.*, 2002, 2004, 2008; *Boynton et al.*, 2002; *Mitrofanov et al.*, 2002].

[3] The polar regions of Mars are dynamic in terms of the transport of water vapor. At Phoenix's latitude, CO_2 and water ice seasonally advance and retreat across the landing site [*Wagstaff et al.*, 2008], providing constant hydrological interaction between the regolith and atmosphere. Mars has a precession cycle of 51 kyr [*Laskar et al.*, 2004]. While aphelion currently is aligned near northern summer solstice, this was not always the case. Model simulations suggest that when perihelion occurs near northern summer solstice, the increased insolation destabilizes the north polar water ice cap. Water ice sublimates from the north polar region and is transferred to the south polar cap, forcing the north circumpolar ice table to be below the surface [*Montmessin et al.*, 2007]. Other simulations also suggest that Mars' large oscillations in axial tilt (obliquities from 0°–45°) shuttles water ice reservoirs between the polar and tropical regions [*Mischna and Richardson*, 2005; *Forget et al.*, 2006; *Montmessin*, 2006]. Such a hydrologically active site throughout the annals of Martian geologic time is ideal for carrying out the mission objectives of Phoenix.

[4] The Phoenix Mission started in late spring (L_s ~77°) and ended in late summer (L_s ~148°), lasting 151 sols [*P. Smith et al.*, 2009]. In situ measurements characterized the local atmospheric conditions (i.e., temperature, pressure, composition, wind, dust and water ice opacities, fogs, ground frosts) [*P. Smith et al.*, 2008, 2009; *Davy et al.*, 2010; *Dickinson*, 2008; *Holstein-Rathlou and Gunnlaugsson*, 2008; *Whiteway et al.*, 2009; *Lemmon*, 2008; *Hecht*, 2008; *Taylor et al.*, 2010; *Tamppari et al.*, 2010; *Zent et al.*, 2010; *Renno et al.*, 2009; *Holstein-Rathlou et al.*, 2010]. Using the NASA Ames Mars General Circulation Model (GCM) version 2.1, we simulate atmospheric conditions at the Mars Phoenix Lander site in an effort to explain various atmospheric phenomena measured by Phoenix, in particular water ice clouds, and ground frosts. We study the reasons why many of these phenomena occur only toward the end of the mission [*Lemmon*, 2008; *Whiteway et al.*, 2009]. The intent of this manuscript is not to imply that the model can predict the weather, but that the model reliably predicts the climate, with differences between the model and data being a function of

[1]Atmospheric, Oceanic, and Space Sciences, University of Michigan, Ann Arbor, Michigan, USA.
[2]Department of Astronomy, New Mexico State University, Las Cruces, New Mexico, USA.
[3]Planetary Science Institute, Tucson, Arizona, USA.

0148-0227/10/2010JE003568

the weather. In section 2, we analyze the atmospheric observations made by Phoenix. Section 3 entails a brief description of the model used in this study. Section 4 presents results of simulations with our GCM, while section 5 includes a discussion of our findings and their implications.

2. Phoenix Observations

2.1. Instrumentation

[5] The Phoenix Lander carried a variety of instruments, which together, gave a clear picture of the high-latitude climate of Mars during late spring and summer. Its meteorological package (MET) measured pressure, temperature, and wind [*Smith et al.*, 2009; *Taylor et al.*, 2008]. Three thermocouples on the MET mast made temperature measurements at heights 0.25, 0.5, and 1.0 m above the lander deck, and the deck was ~1 m above the ground. Wind was calculated from images of a Telltale whose deflection is a function of the wind vector. The wind speed and direction could be measured reliably for speeds smaller than 10 m/s [*Taylor et al.*, 2008; *Holstein-Rathlou et al.*, 2010].

[6] A lidar system onboard the lander measured the vertical profile of atmospheric dust and water ice by measuring laser light backscattered by airborne particles. It had 50 m vertical resolution and was capable of detecting water ice clouds of 0.05 opacity up to 20 km above the lander [*Whiteway et al.*, 2008].

[7] The Surface Stereo Imager (SSI) was located ~2 m above the ground and was a multispectral science camera similar to the Imager aboard Mars Pathfinder [*Smith et al.*, 1997] and Mars Polar Lander's SSI [*Smith et al.*, 2001]. Besides being the camera used to image the Telltale, SSI was capable of measuring atmospheric opacity and scattering. Solar imaging at 451, 671, 887, and 991 nm was used to separate dust and water ice contributions to the atmospheric optical depth, while the 935 nm wavelength provided a measurement of the water vapor column abundance [*Smith et al.*, 2008].

[8] The Thermal and Electrical Conductivity Probe (TECP) was located near the tip of the Robotic Arm and measured temperature and humidity. Measurements near the surface (typically ~5 cm above the ground) could be used to quantify the exchange of water between the regolith and the atmosphere [*Zent et al.*, 2009].

2.2. Observation

[9] Phoenix (MET) measured a steady decline in near-surface atmospheric pressure over the course of the mission resulting from the growth of the CO_2 south polar ice cap. Atmospheric pressure declined from ~8.6 hPa at the beginning of the mission to ~7.2 hPa near its end. This pressure minimum occurred at sol ~135 (L_s ~140°) as was expected from the previous measurements by the Viking mission [*Tillman*, 1988; *Dickinson*, 2008; *Taylor et al.*, 2010]. Atmospheric temperatures at ~2 m above the surface indicated daytime highs of ~245 K and nighttime lows of ~190 K [*Dickinson*, 2008; *Davy et al.*, 2010].

[10] Nighttime clouds were seen regularly after sol 89 (L_s = 117°), but dissipated quickly after sunrise. Clouds consisted of ground fog and a separate cloud deck at 3–6 km [*Whiteway et al.*, 2009, Figure 1b]. As the mission progressed, the clouds endured longer into the morning hours and the cloud deck extended closer to the surface. Clouds were not detected in the afternoon or evening hours [*Whiteway et al.*, 2009; *P. Smith et al.*, 2009]. In the middle of the mission, ground frosts formed sporadically, on sols 79 and 89, and then frequently after sol 110 [*Lemmon*, 2008; *P. Smith et al.*, 2009].

[11] The daily maximum water vapor pressure measured by TECP was ~1.8 Pa at 5 cm above the surface. During the night the vapor pressure dropped below 0.1 Pa. Midsol relative humidity values derived from the vapor pressure and 2 m temperature measurements were ~5%. The detection of ground fogs and low-lying clouds at night suggests the near-surface atmosphere was saturated early in the mission and at mission's end. During the coldest days of the mission, daytime temperatures still remained above the frost point. However, the nighttime temperatures during such days were low enough for the formation of fogs and frosts on the surface [*P. Smith et al.*, 2009; *Hecht*, 2008; *Dickinson*, 2008; *Davy et al.*, 2010; *Zent et al.*, 2009; *Lemmon*, 2008; *Whiteway et al.*, 2009].

[12] Winds measured by the Telltale appear to be relatively repeatable at night with easterlies of ~4 m/s. During the day, the winds are variable, rotating through a full 360° in direction with wind speeds ranging from 1 to 12 m/s. Daytime winds start as easterlies in the morning, rotating to southerlies by midsol and through to westerlies and then northerlies by late afternoon, finally becoming easterlies again in the evening. These winds may be the result of anabatic and katabatic effects [*Holstein-Rathlou and Gunnlaugsson*, 2008; *Holstein-Rathlou et al.*, 2010].

[13] Observations of the Phoenix landing site from MRO's Compact Reconnaissance Imaging Spectrometer for Mars (CRISM) indicate seasonally increasing water vapor column abundance values which increase through L_s ~120° (sol ~95) to a value of ~45–50 pr μm [*M. Smith et al.* 2009; *Tamppari et al.*, 2010]. Then, the water vapor abundances decline until the end of the mission. CRISM also showed short-term variability (<10 sols) with spikes in vapor abundance over the lander increasing by as much as 30% on L_s ~95° and 120°. Near-surface TECP measurements of the water vapor abundance show higher variability than CRISM. This may be due to a nonuniform vertical mixing ratio profile near the lander [*Tamppari et al.*, 2010], or due to spatial and temporal averaging of CRISM spectra smearing out short-term local changes in the vapor abundance [*M. Smith et al.*, 2009].

3. NASA Ames GCM Version 2.1

[14] The NASA Ames Mars General Circulation Model (GCM version 2.1) is a finite difference numerical grid point model of Mars' atmosphere. Current model geophysical processes include the calculation of radiative transfer using a correlated-k approach [*Liou*, 2002]. It accounts for solar and thermal infrared absorption/reemission by CO_2 and suspended dust when determining the radiative heating rates. Dust opacity in the model is prescribed by ingesting the first year of MGS TES 9 μm dust opacity data into the model (a nominally dusty year) [*Smith*, 2004]. For further discussion on how the opacity map is ingested in to the GCM, see *Nelli et al.* [2009]. The model includes the effects of diurnally and seasonally varying insolation, as well as CO_2

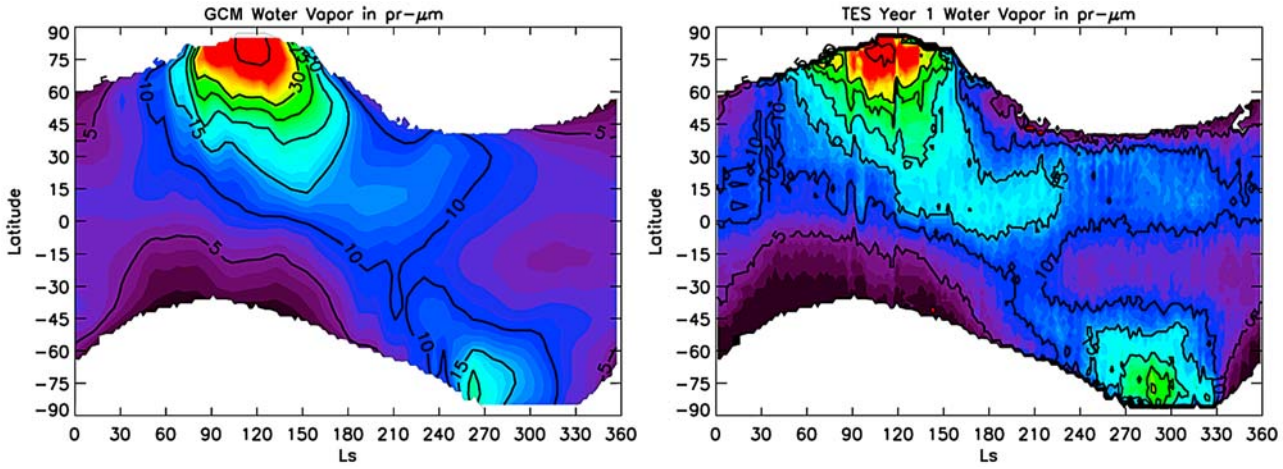

Figure 1. (left) Model-derived zonal mean water vapor abundances in pr μm. (right) TES derived abundances [*Smith*, 2004]. Contours are 5, 10, 15, 20, 25, 30, 50, and 70 pr μm. The white shading over the poles is where the surface temperatures were too cold for TES to obtain accurate values.

condensation/sublimation and explicit boundary layer treatment [*Haberle et al.*, 1993, 1999]. MOLA topography [*Smith et al.*, 1999] and spatially variable thermal inertia and albedo fields based on Viking and Mars Global Surveyor observations (F. Forget, personal communication, 2005) are smoothed to the required model resolution. Aerosol transport and the atmospheric thermodynamic equations are solved on a 5° latitude by 6° longitude Arakawa C grid by the model's dynamical core [*Suarez and Takacs*, 1995].

[15] A surface water ice source is seasonally exposed at the two most northerly model latitudes (every grid point at 85°N and 15 grid points at 80°N) to produce a water ice cap equal in area to that measured [*Zuber et al.*, 1998]. The albedo of the north residual ice cap at 80°N (15 grid points) has been increased by 20% above the observed values to reduce sublimation so as to obtain a water cycle comparable to the latest TES values (Figure 1) [*Smith* 2002, 2004, 2006; *Fouchet et al.*, 2007; M. Smith, private communication, 2007]. Sublimation of water ice off the perennial north polar cap (or from seasonal and nightly deposits) is treated in the same way that *Haberle et al.* [1999] do the turbulent exchange of heat, in which the drag and heat coefficients are calculated in a self-consistent way. Sublimated water is added to the lowest atmospheric layer. Using a moment transfer scheme based on the ideas proposed by *Rodin* [2002] and *Montmessin et al.* [2002, 2004] (and described in greater detail by *Nelli et al.* [2009]), a simplified microphysical treatment for cloud formation is incorporated into the GCM. Water ice precipitation upon the surface occurs via sedimentation of water ice cloud particles through the calculation of the Stokes-Cunningham flow [*Pruppacher and Klett*, 2000] for a spherical particle. The model also accounts for direct deposition of frost onto the surface from the bottom atmospheric layer. Clouds are radiatively inactive. A full description of the hydrological cycle in the GCM, how it is tuned, and how it compares to current observations can be found in the work of *Nelli et al.* [2009].

[16] The Ames GCMv2.1 requires a spin-up time scale of several years in order for dynamical processes to produce a seasonally varying latitudinal gradient in water vapor abundances that is reproducible from year to year. The model is initially started from an isothermal, static state to allow the atmosphere (temperature, pressure, etc.) to adjust to current Martian conditions. Once the GCM water cycle becomes repeatable on a yearly basis, the simulation is stopped and the last year analyzed (year 5 in this study). While in previous years the water cycle had not yet reached a steady state, results from year 5 are repeatable on a qualitative basis. Thus, the results presented in this paper are a robust feature of the Ames GCMv2.1.

4. Results

4.1. Pressure and Temperature

[17] The simulated surface pressures at the model grid nearest to the Phoenix landing site are very similar in magnitude and temporal variation to the observed Phoenix pressures (Figure 2) [*Dickinson*, 2008; *Taylor et al.*, 2010]. Due to the averaged MOLA topography [*Smith et al.*, 1999] in the GCM, the location in the model nearest the Phoenix site is 169 m lower than the actual lander [*P. Smith et al.*, 2009]. To compare the model output with the data, the GCM pressure has been adjusted to the same elevation as the Phoenix Lander, an ~2% reduction in GCM pressures. After adjustment, the simulated surface pressures are 1% smaller than the measured values during the first 30 sols of the mission, but thereafter the comparison improves. The model follows very well the observed seasonal pressure trend until sol ~130, when the GCM pressure develops small-scale variability that is not present in the data. In all, the GCM values reproduce well the pressure variations caused by seasonal changes in atmospheric mass, comparable with previous studies using the Ames GCM [*Murphy et al.*, 1995; *Haberle et al.*, 1999; *Nelli et al.*, 2007]. Looking at the diurnal mean pressure demonstrates the GCM's ability to match the diurnal range of the observed pressure cycle. However, the GCM does have less of the semidiurnal component than that seen in the data. A caveat in the comparison of the pressure values from GCM with Phoenix measurements is that measured values may be off by several hundredths of a hPa because the rapidly changing thermal environment was not fully considered in

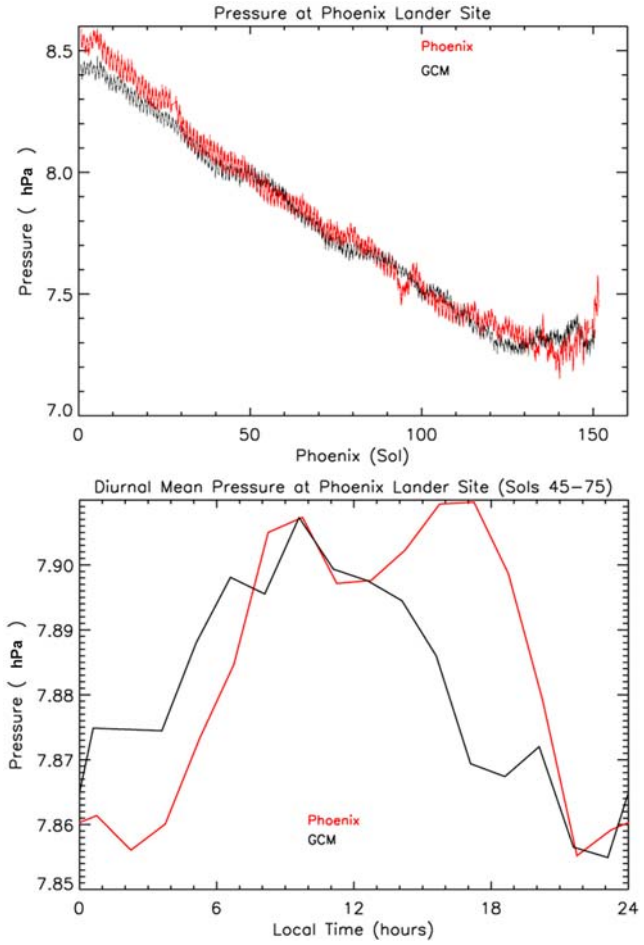

Figure 2. (top) Seasonal pressure trend in hPa at the Phoenix Lander site. Red is the measured daily pressure by the MET package [*Dickinson*, 2008]. The black curve is the simulated pressure in the GCM at the model location nearest the landing site. The GCM pressure has been reduced by ~2% to offset a difference in elevation of 169 m between the model grid point and the actual location of the lander. (bottom) Diurnal mean pressure at the landing site over a 30 sol period near the middle of the mission. The red curve is the data while the black curve is the GCM output.

the comparison of *Taylor et al.* [2010]. This problem does not affect seasonal variations. We tried to mitigate errors in the diurnal mean pressure by averaging over a long period of time (30 sols).

[18] The observed diurnal mean near-surface temperatures ~2 m above the surface at the Phoenix landing site [*Dickinson*, 2008; *Davy et al.*, 2010] and the simulated Phoenix landing site diurnal mean temperatures at a height of ~5 m are presented in Figure 3. The measured temperatures at ~2 m above the surface have larger diurnal amplitude than the simulated temperatures ~5 m above the surface, as expected for a daytime convectively unstable surface layer and nighttime stable boundary layer. One-dimensional (vertical) radiative-convective simulations indicate that the temperatures at 5 m are ~5 K colder/warmer than that at 2 m during the daytime/nighttime, consistent with our GCM simulations. The difference in the temperature range between the data and the GCM is also consistent with Mars Pathfinder data which found an ~8 K difference between the top and bottom thermocouples which were only separated by ~0.75 m [*Schofield et al.*, 1997]. The albedo and thermal inertia in the GCM at the location nearest the Phoenix landing site is similar to, but not the same as, the actual measured values due to the smoothing of the high-resolution surface fields to a 5° × 6° resolution grid. A 10% difference between the measured values for the surface fields and the GCM values can produce a 2–3 K difference in the diurnal temperature range.

4.2. Water Ice Clouds and Frosts

[19] At the GCM's Phoenix location, simulated early morning (0100–0600 LT) water ice clouds (Figure 4) disappear at the beginning of the mission (around sol 10) and do not return until around sol 90. These clouds extend into midmorning (0700–1000 LT) only in the first five simulated sols of the mission (Figure 4) and then do not remain that late in the day again until sol ~100. Finally, the GCM simulations suggest that afternoon (1200–1800 LT) clouds are not present over the landing site until the last ten sols of the mission (Figure 4). The simulations predict that as the season progresses, clouds extend later into morning. By sol 96 (L_s ~120°), a simulated ground fog also forms at night with a separate cloud deck at ~4.5 km (Figure 5). This compares very well with *Whiteway et al.* [2009, Figure 1b]. The simulated ground fog and cloud mass increase as the end of the mission approaches. Little to no simulated frost is expected to be seen ten sols after landing until midmission. Sporadic frosting is seen between sols 50 and 60 in the GCM, and nightly frostings approaching 1 μm in depth begin by sol 90 (Figure 6). The model matches the observed characteristics and seasonality of the atmospheric water ice

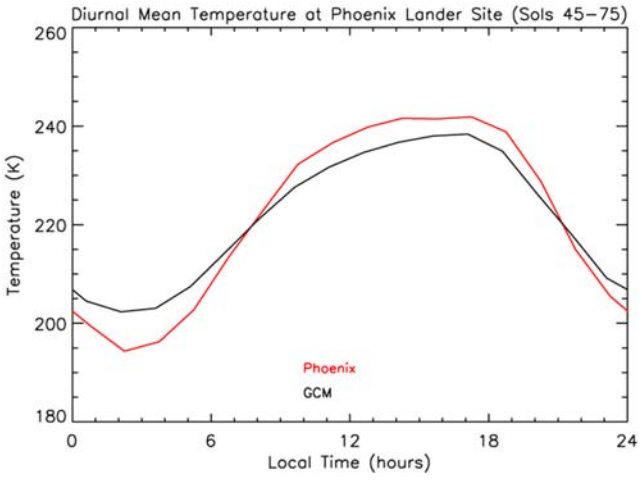

Figure 3. The red curve is the diurnal mean temperature measured by Phoenix at ~2 m above the surface [*Dickinson*, 2008]. The black curve is the GCM simulated diurnal mean temperatures at a location ~5 m above the surface. Differences in the diurnal temperature range between the two curves can be attributed to a difference in height and minor variations in the surface fields between the Phoenix location and the GCM.

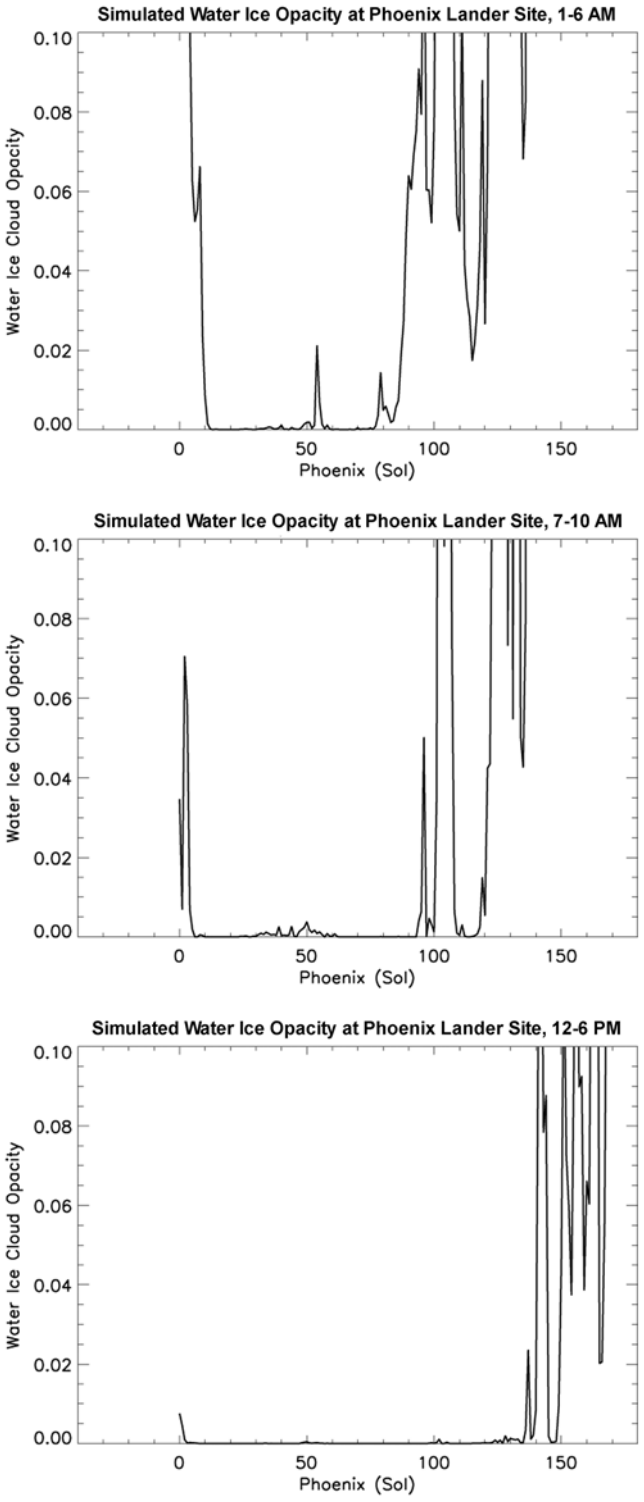

Figure 4. (top) Simulated water ice opacity over the lander site for 0100–0600 LT, (middle) 0700–1000 LT, and (bottom) 1200–1800 LT. Morning clouds begin on sol ~90. As the season progresses, clouds extend later into the morning hours. No clouds are seen in the afternoon hours until the very end of the mission.

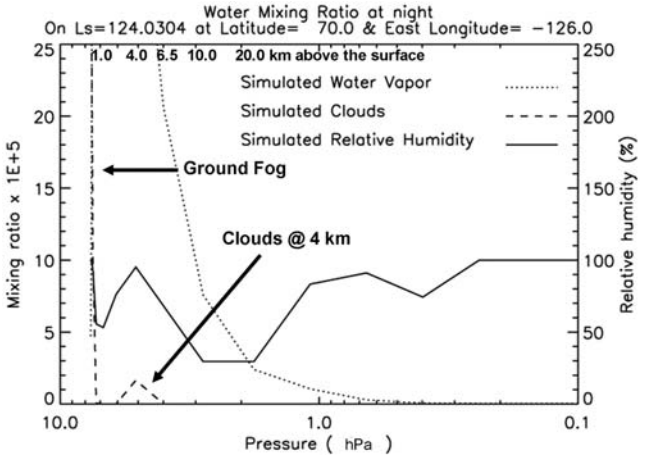

Figure 5. Simulated water vapor and cloud ice mixing ratio over the Phoenix site (mean atmospheric conditions from 0100 to 0600 LT). By L_s ~120° (sol 96), nightly ground fog forms with a separate cloud deck at ~4 km. The atmospheric layer between the ground fog and the cloud deck at the top of the boundary layer (~4–6 km) is cloud free and, thus, the water cloud ice mixing ratio is zero. Same is true for the atmospheric conditions above (>6 km) the boundary layer cloud deck. This compares very well with *Whiteway et al.* [2009, Figure 1b]. Ground fog and clouds increase as the season progresses.

(clouds, fogs, frosts) very well. The one exception is that the simulated sporadic frosting between sols 50 and 60 and the onset of nightly frostings by sol 90 occurs ~20–30 sols earlier than observed (see section 2.2) [*Lemmon*, 2008; *P. Smith et al.*, 2009; *Whiteway et al.*, 2009; *Tamppari et al.*, 2010]. It is not inconsistent that the mission did not see ice clouds during the first 10 sols. The onset of clear skies in the model can vary by 5–10 sols at the beginning of the mission during varying years due to local weather conditions (not shown here). Also, lidar measurements were not taken before 1100 local time until sol 8, and these measurements were still after 0900 local time.

[20] Our results support the conclusions of *Whiteway et al.* [2009]. On the sols surrounding sol 99, the GCM produces a column water vapor abundance of ~45 pr μm, with ~90% of the column abundance located within the PBL. Simulated cloud ice in the column reaches as high as 1.59 pr μm, consistent with the *Whiteway et al.* [2009] derived values. Water vapor sublimated from ice on the surface of (or from cloud ice) and/or advected into the region of the Phoenix Lander is turbulently mixed to the top of the planetary boundary layer (PBL) during the day. At night, clouds form at the top and the bottom of the PBL (where the coolest temperatures are), and water is transported toward the surface via precipitation or placed directly on the surface through deposition. This process confines water within the PBL. This is consistent with results found during the Pathfinder mission, where water vapor was mostly constrained to the bottom 1–3 km of the atmosphere [*Titov et al.*, 1999]. As the height of the PBL changes seasonally with the temperature, so does the PBL's capacity to hold water vapor. Thus, the height of the PBL would be one of the controlling factors in the amount of water in the total column abundance.

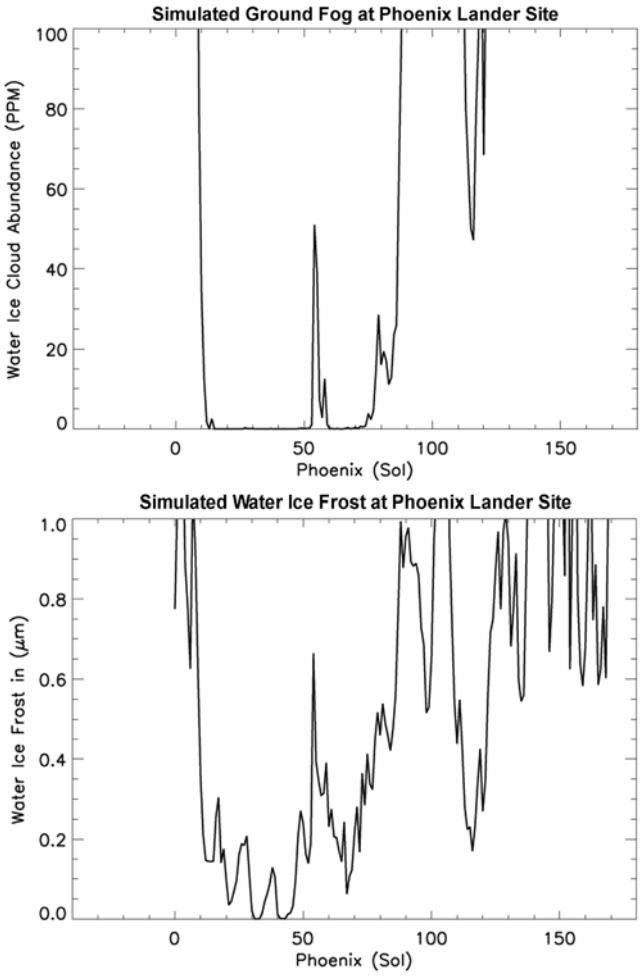

Figure 6. (top) Simulated ground fog formation over the Phoenix site in ppm (0100–0600 LT) and (bottom) daily frost accumulation in μm. The GCM accounts for both water ice cloud precipitation and direct deposition of frost onto the ground. The dramatic increase in ground frost correlates with the sudden and short-lived appearance of a ground fog in the GCM between sols 50 and 60.

This conclusion is consistent with that of *Whiteway et al.* [2009].

4.3. Water Vapor Pressure and Relative Humidity

[21] In our simulations, the daytime maximum water vapor pressure varies between 0.3 and 1.3 Pa, with a mean value of ~0.7 Pa. At night, the simulated vapor pressures are between 0.1 and 0.01 Pa. The nighttime simulated values match the data well (but contain a larger range in pressure values), while the simulated daytime maximum vapor pressure is 40–50% lower than the measured values shown in Figure 7. The difference in the daytime vapor pressure between the GCM and the data can be attributed to the fact that the GCM values are at ~5 m above a regolith without ground ice, while at the landing site exposed ice sublimates during the day and might affect the humidity measurements done as low as 5 cm above the surface. The simulated near-surface relative humidity reaches 100% at night, with midsol values varying between 2% and 30%. Like the Phoenix measurements, the simulated midsol relative humidity values are well below saturation [*Smith et al.*, 2009; *Hecht*, 2008; *Zent et al.*, 2009].

[22] The lack of ground ice imposes no serious constraint on the GCM because it simulates ice accumulation by precipitation, frost formation, and ice sublimation. Indeed, the GCM is capable of reproducing not only the column water vapor abundance, but also clouds, fogs, and frosts measured by the lander. Perhaps, the only limitation that not having ground ice imposes on the GCM is that it produces water vapor pressures at midday over the lander at 50–60% of the measured value. If not for the exposure of subsurface ground ice to the atmosphere by the lander (through the mechanical removal of a 4–5 cm thick layer of regolith), the water vapor pressures measured by the TECP would most likely be closer to the GCM produced values.

4.4. Surface Winds

[23] The near-surface model winds provide the least favorable comparison of all the atmospheric data sets. The GCM values do not match the observed direction well (Figure 8). Observations show the wind directions progressing through a full 360 degrees from midmorning to midafternoon. The GCM wind directions rarely progress through more than 180 degrees, and typically lack winds from the south. This probably occurs because the GCM resolution is not large enough to capture local slope flow or katabatic winds [*Holstein-Rathlou and Gunnlaugsson*, 2008; *Holstein-Rathlou et al.*, 2010]. The lowest level winds (~2 m observed, ~5 m in the GCM) are strongly affected by local topography and are not necessarily representative of the large-scale winds [*Nelli et al.*, 2009]. Since the GCM is not able to reproduce the observed winds, probably because of local topographical effects, mesoscale models needs to be used to address this issue.

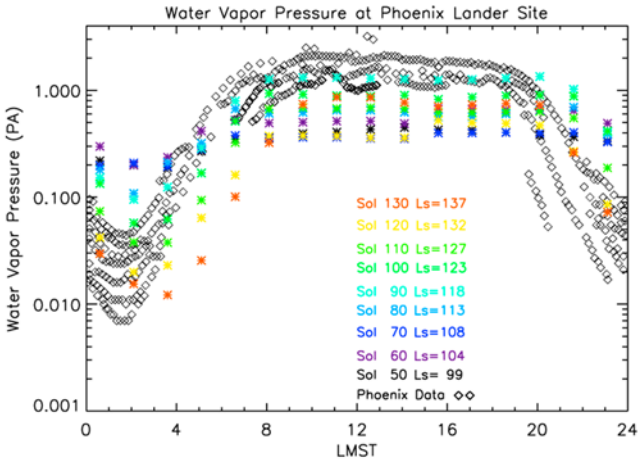

Figure 7. Measured water vapor pressure at the Phoenix site (black diamonds) [*P. Smith et al.*, 2009; *Hecht*, 2008] and simulated water vapor pressure (asterisks colored for specific L_s) in Pa. The data spans L_s ~80°–140°. Both the data and the GCM reach a steady maximum pressure between the hours of 0800 and 1800, with the pressure bottoming out in the early hours of the morning.

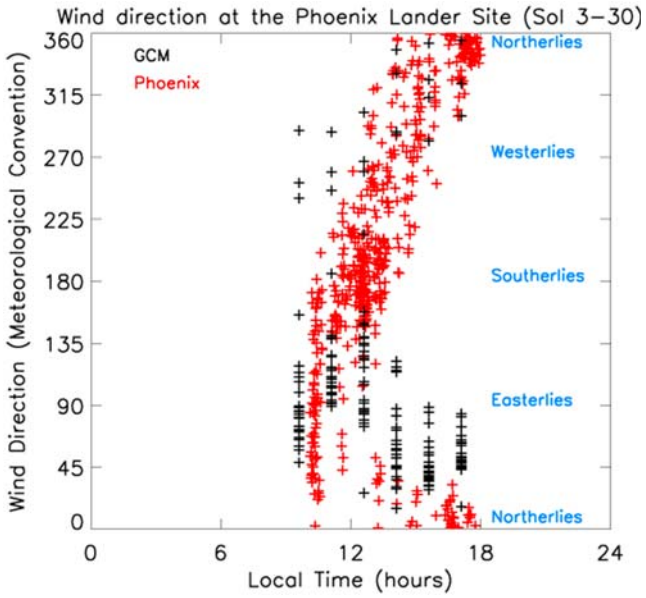

Figure 8. Measured (red crosses) [*Holstein-Rathlou and Gunnlaugsson*, 2008; *Taylor et al.*, 2008; *Holstein-Rathlou et al.*, 2010] and simulated (black crosses) near-surface winds over the Phoenix site. The GCM shows a characteristic lack of southerlies. This is most likely attributed to the lack of resolution of Heimdall crater in the GCM.

4.5. Column Water Vapor

[24] Our GCM simulations produce a general increase in atmospheric water vapor content above the Phoenix landing site until sol ~95 (L_s ~120°) as indicated in Figure 9. After this time, the decreasing sunlight, and hence cooler surface temperatures, reduces the amount of sublimation off the polar cap [*Smith*, 2004]. While the simulated atmospheric water vapor content generally increases over the lander until sol ~95 (L_s ~120°), there are perturbations superimposed upon the general temporal increase. These perturbations are evident in other years of the GCM simulation, suggesting repeatability caused by summer atmospheric phenomena. The water vapor content over the landing site presents a sharp peak near sol 5 in all years of our simulations, due to the removal of the last vestiges of the seasonal CO_2 ice veneer from the seasonal groundwater ice at latitudes just north of the lander. Seasonal water ice (deposited the previous autumn) is being sublimated from the adjacent grid point north of the lander from sol ~−10 to sol ~10, and some of the vapor is subsequently transported southward over the lander. The water vapor presents another sharp peak sometime between sols 50 and 80, depending on the year. A third peak of atmospheric water vapor concentration occurs between sols 90 and 100. This last peak corresponds to the seasonal peak of water vapor over the north polar cap. The peaks in the water vapor abundance correspond to peaks in the ice clouds and frosts generated by the model.

[25] The occurrence of the simulated water ice clouds, fogs, and frosts at the Phoenix location are controlled by temporal maxima in the local water vapor abundance; these maxima in column vapor abundance exceed 50 pr μm. In section 5 we present an analysis of the simulated transport processes responsible for the decrease in local water abundance (and cloud/frost occurrence) shortly after landing, the recurrence of increased water abundance (and sporadic frosting/fogs) in the sol 50–80 time interval, and the subsequent return of nightly frostings/fogs at mission's end.

5. Discussion

5.1. Meridional Transport

[26] We now analyze regional-scale weather events near the Phoenix landing site in order to study their influence on the local column abundance of water vapor. The simulated water vapor column abundance and wind vectors at the 4 hPa pressure level above the region surrounding the landing site (marked by a black 'X'), every 10 sols, are presented in Figure 10. The ten images in Figure 10 cover the three simulated peaks in water vapor over the site, as well as the periods of relatively low vapor abundance between them. Most of the simulated water vapor and cloud ice is confined below the 3–4 hPa level in the model, therefore the 4 hPa wind vectors provides a good indication of the flow of simulated atmospheric water in the polar region. The landing site is located north of the Tharsis rise and NNW of Alba Patera. In the GCM dry air from Tharsis is frequently transported northward toward the landing site. The simulated winds shift in magnitude and direction near sol ~50, and dry air off Tharsis no longer penetrates over the landing site. This allows the simulated water vapor column abundance to increase to more than 50 pr μm over the landing site as moist airflows southward from the cap.

[27] Figure 11 shows simulated meridional wind direction and magnitude averaged daily for three latitudes in the GCM located along the meridian that lies closest to Phoenix's landing site (70°N, 234°E in the GCM lies closest to the Phoenix landing site). During the sols 15–50 time interval, the simulated meridional wind is advecting northward from ~60°N, across the lander toward the pole. These southeasterlies advect dry air from Tharsis and Alba Patera toward the landing site. Near sol 50, the simulated meridional

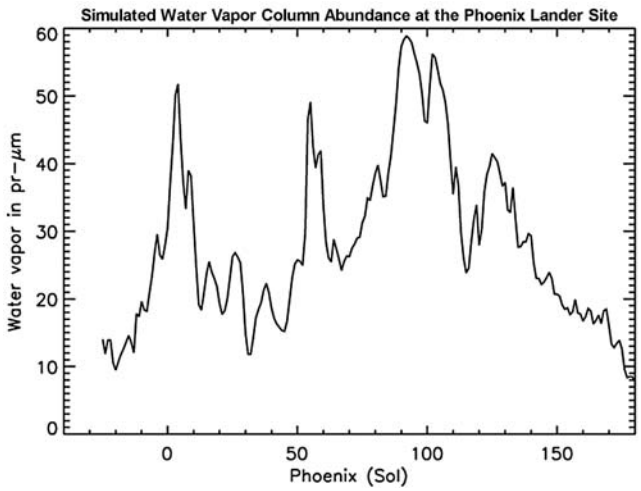

Figure 9. Simulated water vapor over the Phoenix site in pr μm. Water vapor over the site generally increases until sol 96 (L_s ~102°), but large deviations exist over short time scales (i.e., sols ~5 and ~55).

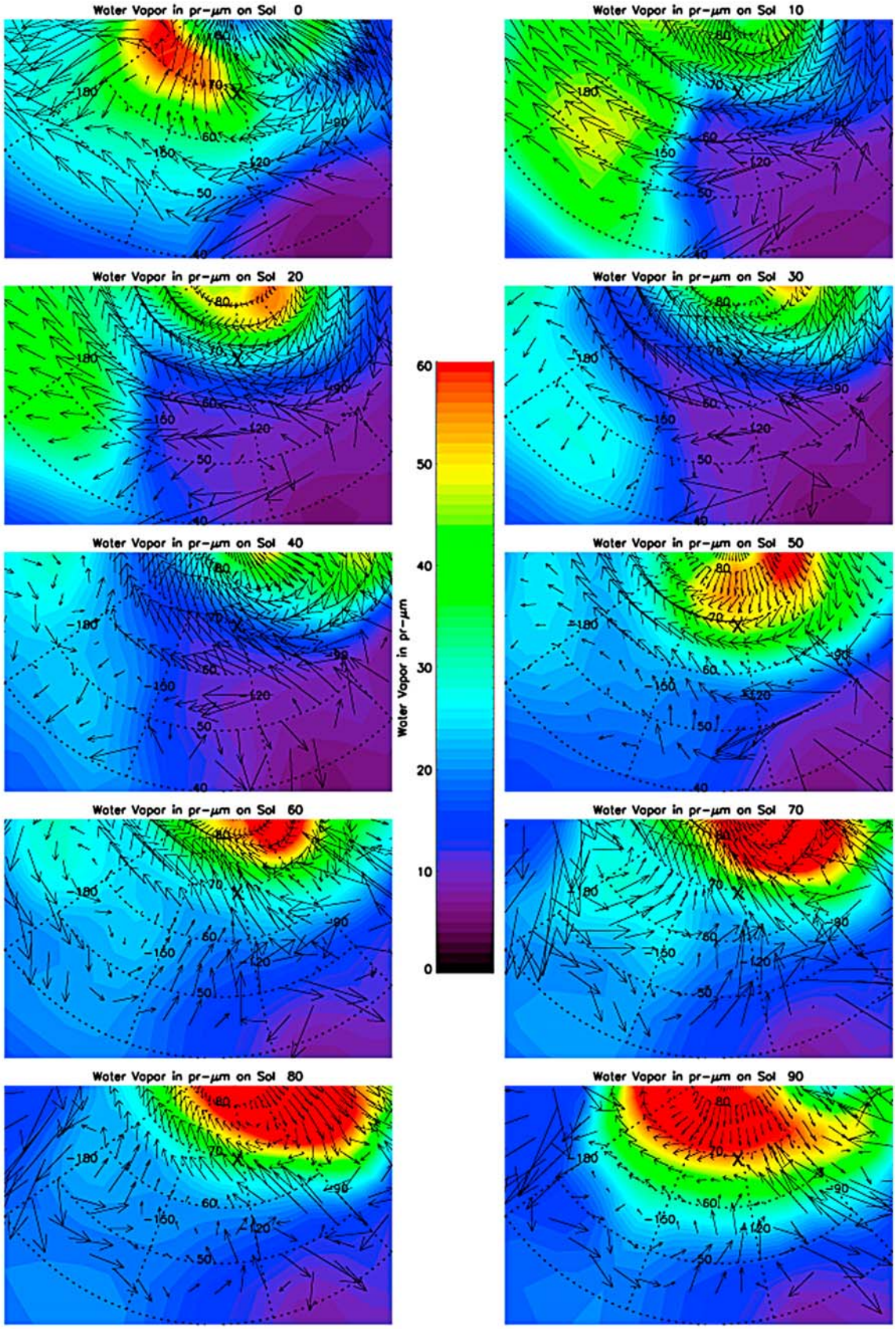

Figure 10. Simulated water vapor (pr μm) and wind vectors (at 4 hPa) over the Phoenix quadrant. Each image represents a daily mean and is separated by 10 sols in time. Wind vectors are taken at 4 hPa since most of the atmospheric water is contained below this pressure height in the polar region.

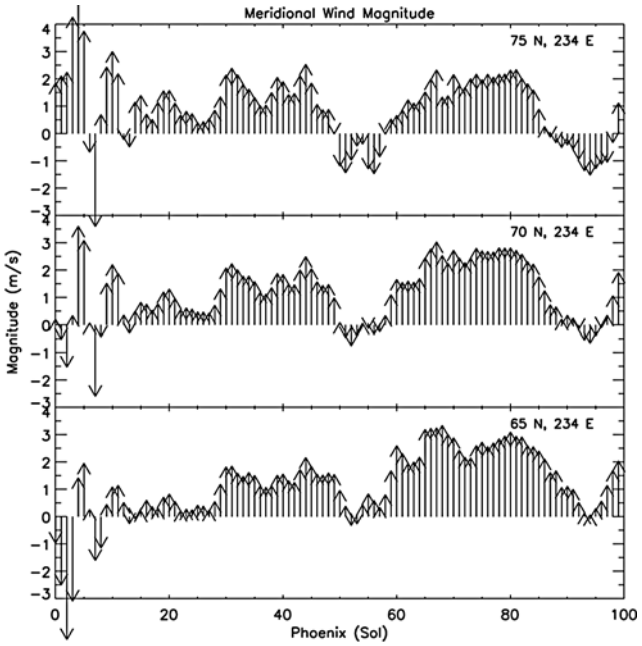

Figure 11. Simulated meridional wind direction and magnitude (at 4 hPa) averaged daily for the three latitudes surrounding the landing site in the GCM at the Phoenix meridian. The middle image is the latitude in the GCM closest to the Phoenix Lander. Atmospheric mass is transported from south to north along the Phoenix meridian except near sols 5, 50, and 90. At this time, a strong northerly prevents the transport of dry air off Tharsis over the lander.

wind abruptly shifts southward. Moist air off the pole is transported south over the lander, hence the build up of water vapor over the landing site in the GCM simulation. After sol 60, the simulated meridional circulation reverts to its presol 50 direction, advecting dry air over the lander. Once more, at sol ~85, strong northerlies off the pole penetrate southward over the Phoenix Lander, raising the simulated water vapor content to seasonal highs. As suggested in Figure 10, Figure 11 shows that simulated northward meridional transport of dry air over the lander is shut off between sols 50 and 60, and again near sol ~90. The weather events that accompany the shift in simulated wind direction during these sols will be discussed below.

5.2. Transient Circulations

[28] While the winter season is known for the occurrence of migrating weather systems [*Banfield et al.*, 2004; *Barnes*, 2006; *Nelli et al.*, 2007], high summer hemisphere latitudes can also experience similar types of weather phenomena caused by baroclinic instabilities in this region of large meridional temperature gradients. To isolate the pressure signature of simulated weather systems passing over the lander location during the first 100 sols of the Phoenix mission, a linear least squares fit was applied to the daily mean GCM simulated pressure values. The simulated daily mean pressure computed from the least squares fit was then subtracted from the simulated pressures and the pressure perturbation versus time investigated (Figure 12). This analysis indicates that temporally low pressure was experienced beginning on sol 30 of the GCM simulation. This low-pressure time interval, with a perturbation pressure minimum at simulated sol 40, is concurrent with simulated relatively dry conditions at the lander location, suggesting that the winds associated with the low-pressure system transported drier air from the south over the landing site (Figure 13). Starting at sol 40, the simulated pressure perturbation at the landing site increases, accompanied by an increase in the simulated water column abundance, which reaches a maximum (as does the pressure) at sol ~55. Subsequently, simulated perturbation pressures near the landing site again declines, accompanied by a reduction in the simulated column water vapor abundance (Figure 13). These temporal variations of perturbation pressure and water vapor are consistent with the propagation of "high-" and "low"-pressure systems and their accompanying wind fields, which change the meridional transport of water vapor.

[29] Determination of perturbation pressures from the Phoenix measurements was conducted using the method applied to the GCM simulations. The temporal variation of the measured pressure perturbation is quite similar to the GCM values (Figure 12). The simulated and observed perturbation amplitudes are similar, though there are some differences in time of occurrence of maximum and minimum values as expected. In the simulation, sporadic frosting occurs in conjunction with the occurrence of the sol 55 peak pressure perturbation, but frost occurrence then declines until perturbation pressures again increase between sols 80 and 90. Sporadic frosting was observed by Phoenix in conjunction with the observed perturbation pressure maximum that occurs during the sol 80–90 time interval [*Lemmon*, 2008; *P. Smith et al.*, 2009; *Tamppari et al.*, 2010], but occurrences of frost subsequently decline as the perturbation pressure declined.

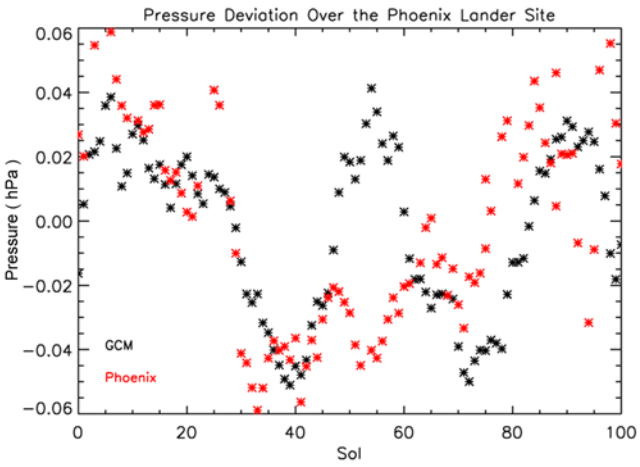

Figure 12. Observed (red asterisks) and simulated (black asterisks) pressure deviations from a linear least squares fit to the first 100 sols. The GCM sees sporadic frostings on sol ~55 and Phoenix reports sporadic frostings on sols 79 and 89. These sols correlate with high-pressure systems moving over the Phoenix landing site in the GCM and the data, respectively.

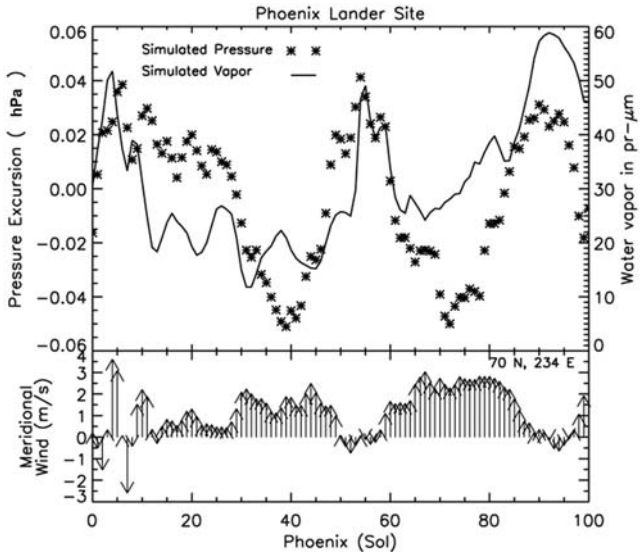

Figure 13. Simulated water vapor (pr μm), pressure excursions (hPa), and meridional wind vectors (m/s) over the Phoenix Lander in the GCM. Maxima in water vapor correlate with maxima in the pressure excursions. Winds associated with the high-pressure excursions transport moist air from the pole over the lander.

[30] We calculate the instantaneous, zonally asymmetric part of the time average simulated surface pressure (p′*) following *Peixoto and Oort* [1992] and plot the daily mean value in order to illustrate simulated pressure deviations spatially across the north polar region. This term represents the traveling high- and low-pressure systems given on terrestrial weather maps. We begin by calculating the deviation from the temporal mean of the surface pressure at each grid point:

$$p'_{(lat,long,t)} = p_{(lat,long,t)} - \overline{p}_{(lat,long)} \quad (1)$$

Here, p is the surface pressure, (overbar) is a temporal mean over 20 sols, and (′) represents the deviation from the temporal mean. Then, we calculate the deviation from the zonal mean of p′:

$$p'^{*}_{(lat,long,t)} = p'_{(lat,long,t)} - [p'_{(lat,long,t)}] \quad (2)$$

Here, [ ] is a zonal mean and (*) represents deviation from the zonal mean quantity.

[31] Applying this pressure perturbation analysis to simulated surface pressures at model grid locations throughout the northern hemisphere, the zonal structure of the high- and low-pressure systems is highlighted (Figures 14 and 15). In Figure 14, on simulated sol 10 (L_s = 81°), a zonal wave number two is evident, consistent with the wave number two synoptic structure generated by *Tyler et al.* [2008] in a mesoscale model simulation for the same season (L_s = 82.5°). *Tyler et al.* [2008] state that these systems usually do not last more than ~5 sols. In our model, the lifetime of this system is similar. The amplitudes of our perturbations are ~1.0% of the surface pressure in the GCM versus an ~2% excursion in the work of *Tyler et al.* [2008]. The amplitude of the perturbations for the two calculations is not exactly the same, but that is expected since we used a different calculation to represent a similar quantity provided by *Tyler*

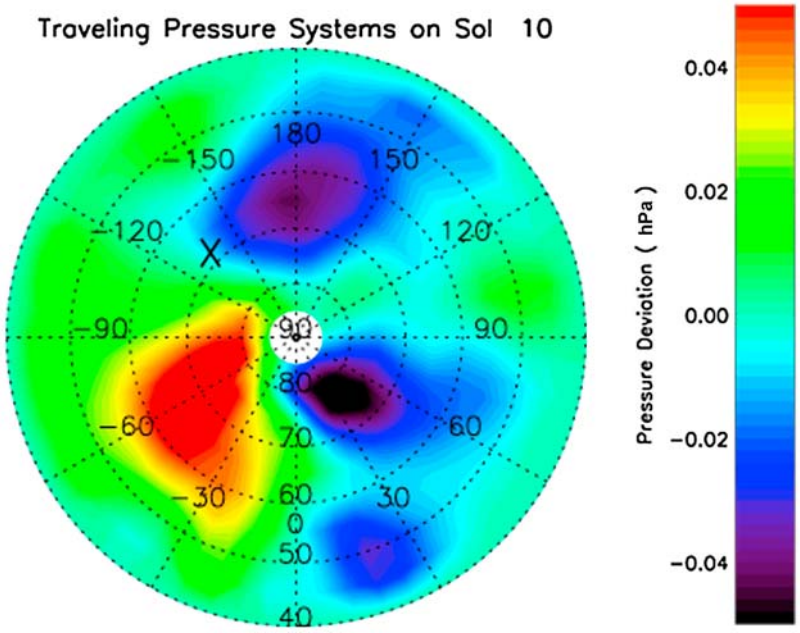

Figure 14. Simulated pressure deviations (hPa) calculated according to *Peixoto and Oort* [1992] for the whole of the north polar region so that zonal structure is made apparent. The zonal wave number 2 pressure system seen on sol 10 (L_s = 81°) has a similar period to the synoptic wave number 2 structure produced by the *Tyler et al.* [2008] mesoscale model during the same time period.

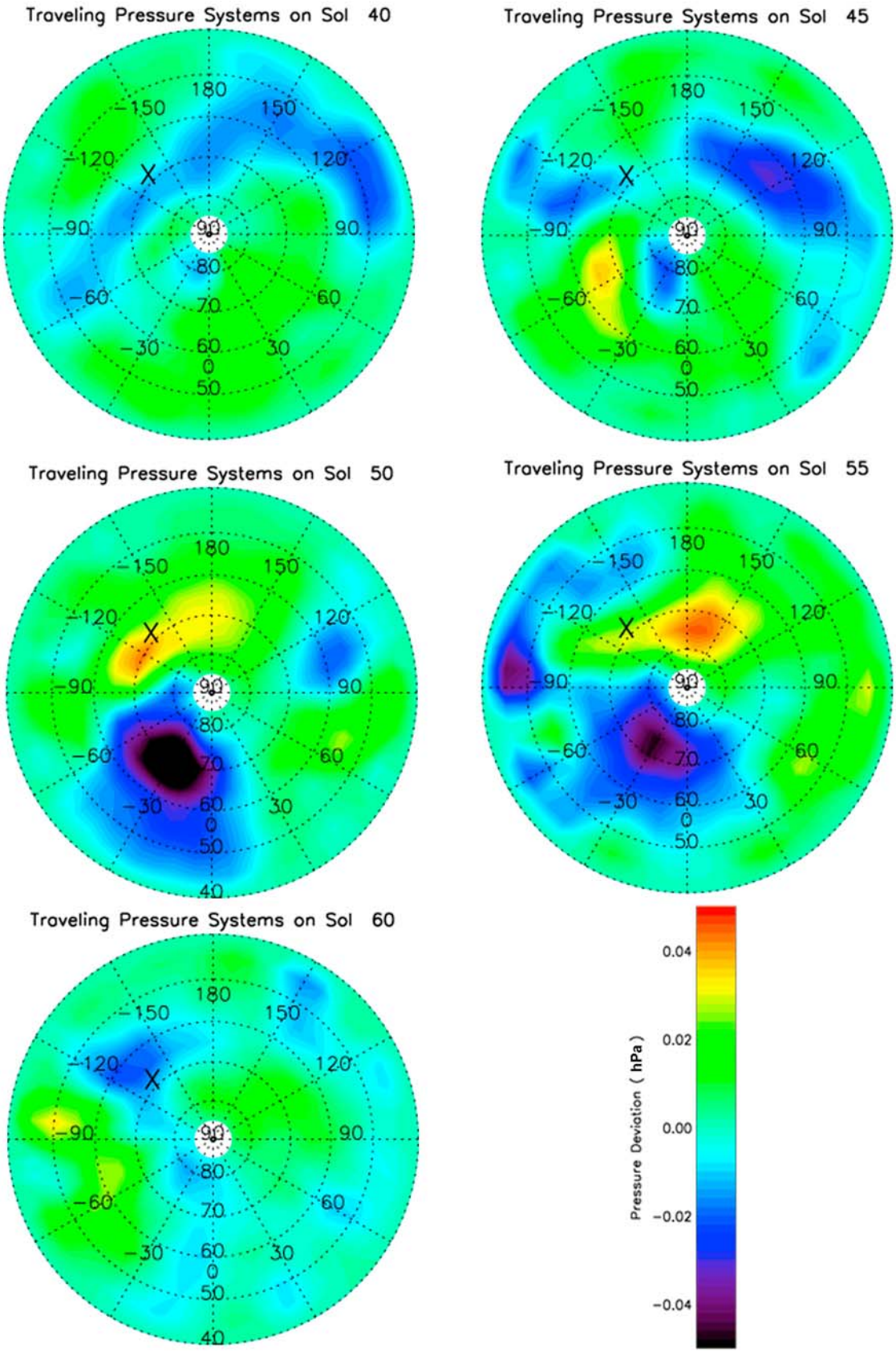

Figure 15. Simulated pressure deviations (hPa) calculated according to *Peixoto and Oort* [1992] for sols 40–60. A high-pressure ridge south of the lander on sol 40 transports dry air over the lander. A low-pressure system moving west toward the lander from sols 50–57 imparts northerly flow over the lander.

et al. [2008]. We used the *Peixoto and Oort* [1992] formulation because it does a better job removing biases in the surface pressure due to topography and CO_2 condensation in the Ames GCM. Nevertheless, these results suggest that the Ames GCM simulates the large-scale atmospheric systems seen in mesoscale models and it provides confidence in the results of our GCM simulations.

[32] Figure 15 provides several snapshots of the simulated pressure systems moving around the lander ('X' location) from sols 40–60. On sol 40, a high-pressure ridge sits just south of the lander. Advection across this ridge is transporting dry air off of Tharsis and over the lander. This high pressure moves north and west over the lander. From sols 50–57, a large magnitude low-pressure system is moving from the east toward the lander, imparting northerly flow of moist air over the lander. During this time period the high-pressure center starts to decline in intensity. After sol 57, the low-pressure system begins moving over the lander itself and atmospheric transport reverts back to presol 50 conditions. During the first 10 sols of the mission in the GCM, pressure systems appear stagnant with a possible weak westward migration of ~15° per day, in contrast to *Tyler et al.* [2008] results.

[33] The simulated dynamics discussed in sections 5.1 and 5.2 are repeatable throughout multiple simulated Mars years. Temporal and spatial variations occur interannually regarding these atmospheric phenomena. The timing of these events has been seen to shift by 30 sols in other years in the GCM. The dynamics leading to these abrupt atmospheric phenomena are climatologically repeatable in the GCM; the exact timing of these events is not, due to weather.

5.3. Summary

[34] Phoenix provided a fabulous data set of high-latitude atmospheric measurements, a region never before studied from the surface of Mars. The Ames GCM was used to simulate atmospheric conditions over the Phoenix landing site in an attempt to understand Phoenix-observed atmospheric phenomena involved in the water cycle, such as the seasonality of water ice clouds, fogs, and frosts. The GCM reproduced a number of atmospheric processes ranging from local temperature and pressure variations to the occurrences of water vapor, ice, and frosts. The GCM predicts the observed sporadic frostings that occur in the middle of the Phoenix mission, followed by more regularly occurring frostings tens of sols later. The simulation results indicate that the occurrence of clouds at the Phoenix landing location is controlled by regional atmospheric circulation systems that alternately transport moist air from the north (poleward direction) and dry air from the south (from Tharsis). The formation of ground fogs and frosts is related to high-pressure systems that form over the landing site and block cool, dry air from Tharsis. When these high-pressure systems dissipate, dry air from Tharsis flows toward the landing site, reducing the local amount of atmospheric vapor and, hence, the condensation rate of water vapor.

[35] **Acknowledgments.** We would like to thank Melinda Kahre and John Wilson for their helpful discussion concerning modeled aerosols and baroclinic systems during northern summer. Also, we thank Mike Hecht and Troy Hudson for providing TECP measurements. We are grateful to the entire Phoenix team, and especially the MET team, for their dedication to this mission and their overwhelming success. Finally, we thank the Editor (Robert Carlson) and reviewers, whose comments have improved this paper immensely. Support for this research was provided by NASA Planetary Atmospheres Programs (NNX09AF23G). Nilton Renno was partially funded by the Phoenix mission and NSF award ATM 0622539.

References

Banfield, D., B. J. Conrath, P. J. Gierasch, R. J. Wilson, and M. D. Smith (2004), Traveling waves in the Martian atmosphere from MGS TES nadir data, *Icarus*, *170*, 365–403, doi:10.1016/j.icarus.2004.03.015.

Barnes, J. R. (2006), FFSM studies of transient eddies in the MGS TES temperature data, paper presented at Second Workshop on Mars Atmosphere Modeling and Observation, 27 Feb.–3 March, Granada, Spain. (Available at http://www-mars.lmd.jussieu.fr/granada2006/.)

Boynton, W. V., et al. (2002), Distribution of hydrogen in the near-surface of Mars: Evidence for subsurface ice deposits, *Science*, *297*, 81–85, doi:10.1126/science.1073722.

Davy, R., J. A. Davis, P. A. Taylor, C. F. Lange, W. Weng, J. Whiteway, and H. P. Gunnlauggson (2010), Initial analysis of air temperature and related data from the Phoenix MET station and their use in estimating turbulent heat fluxes, *J. Geophys. Res.*, *115*, E00E13, doi:10.1029/2009JE003444.

Dickinson, C. D. (2008), PHX meteorological data V1.0, PHX-M-MET-3-PT-RDR-V1.0, NASA Planet. Data Syst., Greenbelt, Md.

Feldman, W. C., et al. (2002), Global distribution of neutrons from Mars: Results from Mars Odyssey, *Science*, *297*, 75–78, doi:10.1126/science.1073541.

Feldman, W. C., et al. (2004), Global distribution of near-surface hydrogen on Mars, *J. Geophys. Res.*, *109*, E09006, doi:10.1029/2003JE002160.

Feldman, W. C., J. L. Bandfield, B. Diez, R. Elphic, S. Maurice, and S. M. Nelli (2008), North to south asymmetries in the water-equivalent hydrogen distribution at high latitudes on Mars, *J. Geophys. Res.*, *113*, E08006, doi:10.1029/2007JE003020.

Forget, F., R. M. Haberle, F. Montmessin, B. Levrard, and J. W. Head (2006), Formation of glaciers on Mars by atmospheric precipitation at high obliquity, *Science*, *311*, 368–371, doi:10.1126/science.1120335.

Fouchet, T., et al. (2007), Martian water vapor: Mars Express PFS/LW observations, *Icarus*, *190*, 32–49, doi:10.1016/j.icarus.2007.03.003.

Haberle, R. M., H. C. Houben, R. Hertenstein, and T. Herdtle (1993), A boundary-layer model for Mars: Comparison with Viking Lander and entry data, *J. Atmos. Sci.*, *50*, 1544–1559, doi:10.1175/1520-0469(1993)050<1544:ABLMFM>2.0.CO;2.

Haberle, R. M., M. M. Joshi, J. R. Murphy, J. R. Barnes, J. T. Schofield, G. Wilson, M. Lopez-Valverde, J. L. Hollingsworth, A. F. C. Bridger, and J. Schaeffer (1999), General circulation model simulations of the Mars Pathfinder atmospheric structure investigation/meteorology data, *J. Geophys. Res.*, *104*, 8957–8974, doi:10.1029/1998JE900040.

Hecht, M. H. (2008), Phoenix MECA non-imaging reduced data V1.0, PHX-M-MECA-4-NIRDR-V1.0, NASA Planet. Data Syst., Greenbelt, Md.

Holstein-Rathlou, C., and H. P. Gunnlaugsson (2008), Phoenix Mars Lander telltale wind velocity and direction data, PHX-M-TT-5-WIND-VEL-DIR-V1.0, NASA Planet. Data Syst., Greenbelt, Md.

Holstein-Rathlou, C., et al. (2010), Winds at the Phoenix landing site, *J. Geophys. Res.*, *115*, E00E18, doi:10.1029/2009JE003411.

Laskar, J., A. C. M. Correia, M. Gastineau, F. Joutel, B. Levrard, and P. Robutel (2004), Long term evolution and chaotic diffusion of the insolation quantities of Mars, *Icarus*, *170*, 343–364, doi:10.1016/j.icarus.2004.04.005.

Lemmon, M. (2008), Phoenix Mars Surface Stereo Imager EDR V1.0, PHX-M-SSI-2-EDR-V1.0, NASA Planet. Data Syst., Greenbelt, Md.

Liou, K. N. (2002), *An Introduction to Atmospheric Radiation*, *Int. Geophys. Ser.*, vol. 84, Academic, San Diego, Calif., doi:10.1016/S0074-6142(02)80015-8.

Mischna, M. A., and M. I. Richardson (2005), A reanalysis of water abundances in the Martian atmosphere at high obliquity, *Geophys. Res. Lett.*, *32*, L03201, doi:10.1029/2004GL021865.

Mitrofanov, I., et al. (2002), Maps of subsurface hydrogen from the high energy neutron detector, Mars Odyssey, *Science*, *297*, 78–81, doi:10.1126/science.1073616.

Montmessin, F. (2006), The orbital forcing of climate changes on Mars, *Space Sci. Rev.*, *125*, 457–472, doi:10.1007/s11214-006-9078-x.

Montmessin, F., P. Rannou, and M. Cabane (2002), New insights into Martian dust distribution and water-ice cloud microphysics, *J. Geophys. Res.*, *107*(E6), 5037, doi:10.1029/2001JE001520.

Montmessin, F., F. Forget, P. Rannou, M. Cabane, and R. M. Haberle (2004), Origin and role of water ice clouds in the Maritan water cycle

as inferred from a general circulation model, *J. Geophys. Res.*, *109*, E10004, doi:10.1029/2004JE002284.

Montmessin, F., R. M. Haberle, F. Forget, Y. Langevin, R. T. Clancy, and J.-P. Bibring (2007), On the origin of perennial water ice at the south pole of Mars: A precession-controlled mechanism?, *J. Geophys. Res.*, *112*, E08S17, doi:10.1029/2007JE002902.

Murphy, J. R., J. B. Pollack, R. M. Haberle, C. B. Leovy, O. B. Toon, and J. Schaeffer (1995), Three dimensional numerical simulations of Martian global dust storms, *J. Geophys. Res.*, *100*, 26,357–26,376, doi:10.1029/95JE02984.

Nelli, S. M., J. R. Murphy, A. L. Sprague, W. V. Boynton, K. E. Kerry, D. M. Janes, and A. E. Metzger (2007), Dissecting the polar dichotomy of the noncondensable gas enhancement on Mars using the NASA Ames Mars General Circulation Model, *J. Geophys. Res.*, *112*, E08S91, doi:10.1029/2006JE002849.

Nelli, S. M., J. R. Murphy, W. C. Feldman, and J. R. Schaeffer (2009), Characterization of the nighttime low-latitude water ice deposits in the NASA Ames Mars GCM 2.1 under present-day atmospheric conditions, *J. Geophys. Res.*, *114*, E11003, doi:10.1029/2008JE003289.

Peixoto, J. P., and A. H. Oort (1992), *Physics of Climate*, Am. Inst. of Phys., New York.

Pruppacher, H. R., and J. D. Klett (2000), *Microphysics of Clouds and Precipitation*, 416 pp., Springer, New York.

Renno, N. O., et al. (2009), Physical and thermodynamical evidence for liquid water on Mars, *J. Geophys. Res.*, *114*, E00E03, doi:10.1029/2009JE003362115(E1), 2010].

Rodin, A. V. (2002), On the moment method for the modeling of cloud microphysics in rarefied turbulent atmospheres: I. Condensation and mixing, *Sol. Syst. Res.*, *36*, 97–106, doi:10.1023/A:1015266131539.

Schofield, J. T., J. R. Barnes, D. Crisp, R. M. Haberle, J. A. Magalhaes, J. R. Murphy, A. Seiff, S. Larsen, and G. Wilson (1997), The Mars Pathfinder atmospheric structure investigation/meteorology (ASI/MET) experiment, *Science*, *278*, 1752–1758, doi:10.1126/science.278.5344.1752.

Smith, D. E., et al. (1999), The global topography of Mars and implications for surface evolution, *Science*, *284*, 1495–1503, doi:10.1126/science.284.5419.1495.

Smith, M. D. (2002), Annual cycle of water vapor on Mars as observed by the Thermal Emission Spectrometer, *J. Geophys. Res.*, *107*(E11), 5115, doi:10.1029/2001JE001522.

Smith, M. D. (2004), Interannual variability in TES atmospheric observations of Mars during 1999–2003, *Icarus*, *167*, 148–165, doi:10.1016/j.icarus.2003.09.010.

Smith, M. D. (2006), TES atmospheric temperature, aerosol optical depth, and water vapor observations 1999–2004, paper presented at Second Workshop on Mars Atmosphere Modeling and Observation, 27 Feb.–3 March, Granada, Spain.

Smith, M. D., M. J. Wolff, R. T. Clancy, and S. L. Murchie (2009), CRISM observations of water vapor and carbon monoxide, *J. Geophys. Res.*, *114*, E00D03, doi:10.1029/2008JE003288115(E2), 2010.

Smith, P. H., et al. (1997), The imager for Mars Pathfinder experiment, *J. Geophys. Res.*, *102*, 4003–4025, doi:10.1029/96JE03568.

Smith, P. H., et al. (2001), The MVACS Surface Stereo Imager on Mars Polar Lander, *J. Geophys. Res.*, *106*, 17,589–17,607, doi:10.1029/1999JE001116.

Smith, P. H., et al. (2008), Introduction to special section on the Phoenix mission: Landing site characterization experiments, mission overviews, and expected science, *J. Geophys. Res.*, *113*, E00A18, doi:10.1029/2008JE003083.

Smith, P. H., et al. (2009), H_2O at the Phoenix landing site, *Science*, *325*, 58–61.

Suarez, M. J., and L. L. Takacs (1995), Documentation of the AIRES/GEOS dynamical core, Technical report series on global modeling and data assimilation, vol. 5, version 2, *NASA Tech. Memo. 104606*.

Tamppari, L. K., et al. (2010), Phoenix and MRO coordinated atmospheric measurements, *J. Geophys. Res.*, *115*, E00E17, doi:10.1029/2009JE003415.

Taylor, P. A., D. C. Catling, M. Daly, C. Dickinson, H. P. Gunnlaugsson, A.-M. Harri, and C. F. Lange (2008), Temperature, pressure, and wind instrumentation in the Phoenix meteorological package, *J. Geophys. Res.*, *113*, E00A10, doi:10.1029/2007JE003015114(E3), 2009.

Taylor, P. A., et al. (2010), On pressure measurement and seasonal pressure variations during the Phoenix mission, *J. Geophys. Res.*, *115*, E00E15, doi:10.1029/2009JE003422.

Tillman, J. E. (1988), Mars global atmospheric oscillations: Annually synchronized, transient normal mode oscillations and the triggering of global dust storms, *J. Geophys. Res.*, *93*, 9433–9451, doi:10.1029/JD093iD08p09433.

Titov, D. V., W. J. Markiewicz, N. Thomas, H. U. Keller, R. M. Sablotny, M. G. Tomasko, M. T. Lemmon, and P. H. Smith (1999), Measurements of the atmospheric water vapor on Mars by the Imager for Mars Pathfinder, *J. Geophys. Res.*, *104*, 9019–9026, doi:10.1029/1998JE900046.

Tyler, D., J. R. Barnes, and E. D. Skyllingstad (2008), Mesoscale and large-eddy simulation model studies of the Martian atmosphere in support of Phoenix, *J. Geophys. Res.*, *113*, E00A12, doi:10.1029/2007JE003012114(E3), 2009.

Wagstaff, K. L., T. N. Titus, A. B. Ivanov, R. Castano, and J. L. Bandfield (2008), Observations of the north polar water ice annulus on Mars using THEMIS and TES, *Planet. Space Sci.*, *56*, 256–265, doi:10.1016/j.pss.2007.08.008.

Whiteway, J., M. Daly, A. Carswell, T. Duck, C. Dickinson, L. Komguem, and C. Cook (2008), Lidar on the Phoenix mission to Mars, *J. Geophys. Res.*, *113*, E00A08, doi:10.1029/2007JE003002114(E3), 2009.

Whiteway, J., et al. (2009), Mars water ice clouds and precipitation, *Science*, *325*, 68–70.

Zent, A. P., M. H. Hecht, D. R. Cobos, G. S. Campbell, C. S. Campbell, G. Cardell, M. C. Foote, S. E. Wood, and M. Mehta (2009), Thermal and Electrical Conductivity Probe (TECP) for Phoenix, *J. Geophys. Res.*, *114*, E00A27, doi:10.1029/2007JE003052.

Zent, A. P., M. H. Hecht, D. R. Cobos, S. E. Wood, T. L. Hudson, S. M. Milkovich, L. P. DeFlores, and M. Mellon (2010), Initial results from the Thermal and Electrical Conductivity Probe (TECP) on Phoenix, *J. Geophys. Res.*, *115*, E00E14, doi:10.1029/2009JE003420.

Zuber, M. T., et al. (1998), Observations of the north polar region of Mars from the Mars Observer Laser Altimeter, *Science*, *282*, 2053–2060, doi:10.1126/science.282.5396.2053.

S. W. Bougher, S. M. Nelli, and N. O. Renno, Atmospheric, Oceanic, and Space Sciences, University of Michigan, Ann Arbor, MI 48109, USA. (snelli@umich.edu; nrenno@umich.edu; bougher@umich.edu)

W. C. Feldman, Planetary Science Institute, Tucson, AZ 85719-2395, USA. (Feldman@psi.edu)

J. R. Murphy, Department of Astronomy, New Mexico State University, Las Cruces, NM 88003, USA. (murphy@nmsu.edu)